

Modelling of partially-resolved oceanic symmetric instability



S.D. Bachman, J.R. Taylor*

Department of Applied Mathematics and Theoretical Physics, University of Cambridge, United Kingdom

ARTICLE INFO

Article history:

Received 17 February 2014

Received in revised form 28 May 2014

Accepted 18 July 2014

Available online 5 August 2014

Keywords:

Symmetric instability

Ocean modeling

Mixed layer

Restratification

Submesoscale

Eddies

ABSTRACT

A series of idealized numerical models have been developed to investigate the effects of partially resolved symmetric instability (SI) in oceanic general circulation models. An analysis of the energetics of symmetric instability is used to argue that the mixed layer can be at least partially restratified even when some SI modes are absent due to either large horizontal viscosity or coarse model resolution. Linear stability analysis reveals that in the idealized models the amount of restratification can be predicted as a function of the grid spacing and viscosity. The models themselves are used to demonstrate these predictions and reveal three possible outcomes in steady-state: (1) incomplete restratification due to viscosity, (2) incomplete restratification due to resolution, and (3) excessive restratification due to anisotropy of the viscosity. The third outcome occurs even on a high-resolution isotropic grid and in two separate numerical models, and thus appears to be a sort of robust numerical feature. The three outcomes are used to recommend criteria that a successful SI parameterization should satisfy.

© 2014 The Authors. Published by Elsevier Ltd. This is an open access article under the CC BY license (<http://creativecommons.org/licenses/by/3.0/>).

1. Introduction

Regional ocean models are able to resolve smaller-scale features than are normally permitted by climate-scale GCMs. The oceanic submesoscale in particular is a popular topic of study in such models, due to its role as a “bridge” between the large-scale circulation and small-scale flows where mixing and dissipation can occur. Relatively little is known about the dynamics of submesoscale flows because of limitations in computational and observational resources (Capet et al., 2008a), but they are generally understood to have the following characteristics: (1) frontal structures are ubiquitous and are associated with potential and kinetic energy (Spall, 1995; Thomas and Ferrari, 2008; Thomas et al., 2008), (2) a variety of instabilities develop which feed off of the kinetic and/or potential energy and generate submesoscale motions (Mahadevan and Tandon, 2006; Mahadevan, 2006; Capet et al., 2008a,b,c; Fox-Kemper et al., 2008; Klein et al., 2008), (3) the Rossby (Ro) and Richardson (Ri) numbers are $\mathcal{O}(1)$, meaning that balanced models are not appropriate to describe the motion (Molemaker et al., 2005), and (4) submesoscales interact vigorously with other small-scale, high-frequency motions including Langmuir turbulence (Li et al., 2012; Van Roekel et al., 2012) and near-inertial waves (Whitt and Thomas, 2013; Joyce et al., 2013), thereby enhancing the downscale energy cascade.

The role of the submesoscale as an intermediate-scale bridge between the mean circulation and small-scale processes makes its study all the more important. Even in regional models, however, computational limitations affect how much of the submesoscale range can actually be represented in a model – a simulation run at coarse resolution inherently deemphasizes small-scale processes, and a fine-scale simulation with a smaller domain size may miss important interactions between the submesoscale and mesoscale flows. With respect to the small-scale processes, it is an open question as to what resolution is necessary to begin resolving certain types of submesoscale instabilities. The focus of this paper is on the resolvability of one such type of instability, namely symmetric instability (hereafter SI). Research on SI is at an early stage, and to the authors' knowledge no previous studies have systematically explored what resolution is required to resolve it in ocean models.

As computational power increases, models are able to simultaneously resolve a richer set of dynamics by running at higher spatial resolution and incorporating more complex physical and biogeochemical parameterizations. However, higher spatial resolution introduces a new set of challenges as well, the first among these being the issue of double-counting (Delworth et al., 2012). It is commonly thought that as models enter an “eddy-permitting” regime, where some (but not all) of the mesoscale eddies are explicitly resolved, parameterizations should either be turned off or minimized in order to prevent both resolving and parameterizing the same eddies. One reason for this is that parameterizations can out-compete the resolved eddies for the energy sources

* Corresponding author. Address: DAMTP, Centre for Mathematical Sciences, Wilberforce Road, Cambridge CB3 0WA, United Kingdom. Tel.: +44 01223 337030.
E-mail address: J.R.Taylor@damtp.cam.ac.uk (J.R. Taylor).

required to grow, leaving the resolved eddies weak and ineffectual (Henning and Vallis, 2004). Therefore, one of the first steps to developing a skillful parameterization is to know when its use is appropriate, and when it should be turned off to avoid double-counting.

The issue of double-counting is not confined to just mesoscale eddies, however. Submesoscales develop at scales less than 10 km, and these in turn will become partially resolved as GCM resolution becomes even finer in upcoming model generations. SI is one such submesoscale process, and ocean models will increasingly pass into a regime that could be described as “SI-permitting”. As is the case with mesoscale eddies, explicitly resolving only some of the SI modes can be expected to present a challenge in preventing double-counting by a parameterization. As of the writing of this paper no parameterization exists for SI in the oceanic mixed layer, and any forthcoming attempt at one will require knowledge of how SI behaves when it is partially resolved.

Symmetric instability in a stably stratified flow occurs when the Ertel PV takes on the opposite sign of f (Hoskins, 1974). Fronts in the surface mixed layer of the ocean feature strong lateral density gradients, which in conjunction with wind forcing and/or buoyancy fluxes create conditions favorable to the development of SI (Thomas and Taylor, 2010). SI is capable of restratifying the mixed layer on timescales shorter than that of baroclinic instability (Haine and Marshall, 1998; Boccaletti et al., 2007; Li et al., 2012), and both types of instability are central to setting the stratification of the surface ocean at strong fronts.

Energetically, SI can be described as a small-scale shear instability that extracts energy from the vertically-sheared thermal wind (Taylor and Ferrari, 2010; Thomas and Taylor, 2010) and acts as a mediator in the dissipation of oceanic kinetic energy, helping to drive a forward cascade of energy from large to small scales. The term “mediator” is used here because the SI itself is not responsible for dissipation – its length scales are orders of magnitude larger than the dissipation scale, and so it relies on even smaller-scale turbulence to transfer energy downscale to be dissipated. Taylor and Ferrari (2009) showed that finite-amplitude SI develops secondary Kelvin–Helmholtz instabilities along bands of enhanced shear, which then break down into smaller-scale turbulence. However, Kelvin–Helmholtz instabilities are generally understood as 3D processes that are directly resolved in isotropic, very fine-scale simulations such as large-eddy simulations; aside from exceptional circumstances, they would not be resolvable in a regional model with a highly anisotropic grid. This introduces the related question of how and whether SI can restratify the mixed layer in a model when its associated secondary instabilities are not present?

The objective of this paper is to investigate the level of spatial resolution necessary to explicitly resolve SI and to explore how the resolution threshold varies as a function of the mean flow parameters. The spatial scales at which models become SI-permitting are expected to also straddle the threshold between hydrostatic and non-hydrostatic flows; therefore, the resolution requirement is explored in both regimes. The discretization of the grid and the level of model viscosity can also affect the stability of the flow to SI, and so these possibilities are explored as well.

The main text that follows will be subdivided into two sections. The basic stability, energetics, and growth of SI will be discussed in Section 2. The differences between the growth of inviscid and viscously damped SI modes is shown, along with implications about what this may mean for the resolvability of SI in ocean models. Section 3 shows the results from a series of 2D simulations run at various resolutions, illustrating how the post-restratification character of the mixed layer can vary depending on the model viscosity and grid spacing. A summary of the main results and conclusions appears in Section 4. A detailed linear stability analysis of SI can be found in Appendix A.

2. Energetics of SI

The surface ocean is marked by the presence of sharp lateral density gradients formed as a result of frontogenesis. The presence of these lateral gradients modifies the turbulence that arises at the surface due in part to buoyancy loss (Haine and Marshall, 1998) and down-front wind stress (Thomas and Taylor, 2010), and introduces a variety of secondary effects that modulate buoyancy transport through the mixed layer (Thomas and Lee, 2005).

SI can be viewed as a hybrid of convective and inertial instabilities (Haine and Marshall, 1998). Since it is characterized by slantwise motions tilting across the lateral buoyancy gradient, SI is sometimes called “slantwise convection” (Emanuel, 1994). However, as pointed out by Thorpe and Rotunno (1989), SI has many features that are distinctly different from convection. For example, the most unstable motions are often aligned with isopycnals and are associated with a very small buoyancy flux. In fact, while convection is generated through a conversion of potential energy (PE) to kinetic energy (KE) by lowering the center of mass of the fluid, it is possible for SI to raise the center of mass and reduce the vertical stratification. Therefore, to avoid confusion, the term SI will be used rather than slantwise convection throughout the rest of this paper.

SI is one among a hierarchy of hydrodynamical instabilities thought to be prevalent in the ocean mixed layer. It is characterized by perturbations that are independent of the along-front direction. It also differs from baroclinic instability in that it can derive its energy by reducing the geostrophic shear via turbulent Reynolds stresses (Thomas et al., 2013) in addition to extracting PE from the background flow.

The growth of symmetric instability is best understood in terms of the Ertel potential vorticity (PV), which can be defined as

$$q = (f\mathbf{k} + \nabla \times \mathbf{u}) \cdot \nabla b, \quad (1)$$

where here the Coriolis parameter f is a constant under the f -plane approximation. Define the buoyancy frequency $N^2 = \partial b / \partial z$ and the horizontal buoyancy gradient $M^2 = \partial b / \partial x$, taking both to be constant but not necessarily equal to each other. Let the velocity field be $\mathbf{v} = V_B(x) + V_G(z)$, where V_B is a barotropic velocity and V_G the thermal wind velocity in balance with the lateral stratification, so that $dV_G/dz = M^2/f$. Furthermore, assume that the flow is homogeneous in the along-front direction y . The PV for this basic state is $q = (f + \zeta)N^2 - M^4/f$, where $\zeta = dV_B/dx$ is the relative vorticity, and can become negative for a sufficiently strong lateral buoyancy gradient. An alternative criteria for the growth of symmetric instability in such a balanced model is that the bulk Richardson number

$$Ri = \frac{N^2}{\left(\frac{dV_G}{dz}\right)^2} \equiv \frac{f^2 N^2}{M^4} \quad (2)$$

is such that

$$Ri < \frac{f}{f + \zeta} \quad \text{if} \quad f(f + \zeta) > 0. \quad (3)$$

Under these conditions SI is the most unstable mode when $0.25 < Ri < 0.95$ (Stone, 1966, 1970). The stratification throughout most of ocean interior is strong enough to render the flow stable to SI, with the notable exception of the surface and bottom boundary layers (Allen and Newberger, 1998). In the surface mixed layer, conditions for SI to grow are realized by surface forcing that destroys PV until regions of negative PV develop (Thomas, 2005). SI will then quickly restore the fluid to a marginally stable state (Thorpe and Rotunno, 1989) by mixing in fluid of higher PV from either the thermocline or the surface boundary layer. This mixing was discussed at length by Taylor and Ferrari (2009), who showed that SI locally enhances the shear to such an extent that secondary

Kelvin–Helmholtz (KH) instabilities can form, which efficiently mix higher-PV fluid from below. It is less clear, however, how this mixing occurs in models whose grids are too coarse to resolve KH directly. It is therefore useful to consider the growth rate and energetics of SI before proceeding to the modelling analysis.

2.1. Linear theory of SI

Consider a flow with a balanced initial state as above. Linearizing the primitive equations with respect to this initial state and seeking normal mode solutions for the zonal perturbation velocity

$$u' = u_0 e^{ikx + imz + \sigma t}, \quad (4)$$

in an infinite domain, the growth rate for nonhydrostatic, viscous SI with an anisotropic viscosity (Appendix A) is

$$\sigma = \left[\frac{M^4}{N^2} - f(f + \zeta) - N^2 \left(\frac{k}{m} - \frac{M^2}{N^2} \right)^2 \right]^{1/2} \left(\frac{k^2}{m^2} + 1 \right)^{-1/2} - v_h k^2 - v_v m^2. \quad (5)$$

As noted in Taylor and Ferrari (2009), viscous damping acts to suppress the modes with the largest wavenumbers (smallest modes) first. Furthermore, the presence of a nonzero ζ can either stabilize or destabilize the flow when there is cyclonic or anticyclonic rotation, respectively. This can have a strong influence on the growth rate of SI. Indeed, Thomas et al. (2013) found that $\zeta = -0.6f$ on the North Wall of the Gulf Stream, which is strong enough to nearly negate the influence of planetary rotation in (5).

Importantly, in the inviscid limit the growth rate depends on k and m only through the perturbation slope k/m , which yields important information about the orientation of the unstable modes. To explore this, first let $v_h = v_v = 0$, which gives the inviscid growth rate

$$\sigma = \left[\frac{M^4}{N^2} - f(f + \zeta) - N^2 \left(\frac{k}{m} - \frac{M^2}{N^2} \right)^2 \right]^{1/2} \left(\frac{k^2}{m^2} + 1 \right)^{-1/2}. \quad (6)$$

In the limit when $k \ll m$, the growth rate for hydrostatic flow is recovered, from which it is easily seen that the fastest growing modes satisfy

$$\frac{k}{m} = \frac{M^2}{N^2} \quad (7)$$

and are aligned with isopycnal surfaces. Note that this is not the case in the nonhydrostatic limit – the fastest growing modes occur at the slope

$$\frac{k}{m} = \left[1 + \frac{1}{4} \left(\frac{N^2 - f(f + \zeta)}{M^2} \right)^2 \right]^{1/2} - \frac{1}{2} \left(\frac{N^2 - f(f + \zeta)}{M^2} \right), \quad (8)$$

which is shallower than the isopycnal slope when $Ri < f/(f + \zeta)$. In addition to the fastest-growing modes, it is useful to consider the extent of the range of k/m where SI may grow. Setting $\sigma = 0$, one finds that the region unstable to SI is bounded by the slopes

$$\frac{k}{m} = \frac{M^2}{N^2} \pm \frac{f}{N} \sqrt{\frac{1}{Ri} - \left(1 + \frac{\zeta}{f} \right)}. \quad (9)$$

The unstable slopes thus form a wedge, symmetric about the isopycnal slope, where SI can extract energy from the background flow. The mechanism of energy extraction is *not* symmetric about the isopycnal slope, however; SI gains its energy differently depending on which part of the wedge the unstable mode occupies, and parcel excursion theory may be employed to illustrate how this works.

2.2. Parcel excursion theory

Haine and Marshall (1998) used parcel excursion theory to analyze the energetics of a hierarchy of hydrodynamical instabilities. They noted that the extraction of energy from the mean flow by SI is maximized if fluid parcels are exchanged along isopycnals, but they did not focus attention on the energetics of SI modes that are not so aligned. Here the techniques from their analysis are repeated, but with further consideration paid to the full arc of unstable SI modes.

In a zonally invariant model, the absolute momentum is given by

$$\mathcal{M} = v + fx. \quad (10)$$

The absolute momentum is a conserved quantity in inviscid flow with no variations in the y -direction ($D\mathcal{M}/Dt = 0$) and is often used as the determining factor for inertial instability,¹ which itself can be considered a form of SI in the limit where $N^2 = 0$. Assuming thermal wind balance, the slope of the absolute momentum surfaces is

$$\frac{\partial \mathcal{M}}{\partial x} = \frac{\partial v}{\partial x} + f = \frac{f \partial v}{\partial x} + f^2 = \frac{f(f + \zeta)}{M^2}, \quad (11)$$

where again $\zeta = \partial v / \partial x$ is the vertical component of the relative vorticity. If the initial PV is negative (unstable to SI), this implies that

$$Ri = \frac{N^2 f^2}{M^4} < \frac{f}{f + \zeta}, \quad (12)$$

or equivalently that

$$\frac{M^2}{N^2} > \frac{f(f + \zeta)}{M^2}. \quad (13)$$

Then the isopycnal slope is steeper than that of the absolute momentum contours (which for brevity will henceforth be referred to as \mathcal{M} -surfaces), with equality when $Ri = f/(f + \zeta)$ (neutral to SI). For an unstable initial state one can also show that

$$f(f + \zeta)/M^2 > \frac{M^2}{N^2} - \frac{f}{N} \sqrt{\frac{1}{Ri} - \left(1 + \frac{\zeta}{f} \right)},$$

so that the \mathcal{M} -surface always lies within the SI-unstable arc. It is useful to begin by considering the energetics when parcels are exchanged along \mathcal{M} -surfaces.

Haine and Marshall (1998) show that the change in potential energy ΔP due to parcel exchange is given by

$$\Delta P = \rho_0 N^2 \Delta y^2 s \left(s - \frac{M^2}{N^2} \right), \quad (14)$$

where Δy is the horizontal distance of the parcel displacement and s is the slope of the surface along which parcels are exchanged. Similarly, they also showed that the change in kinetic energy ΔK by such an exchange is

$$\Delta K = \rho_0 \Delta y^2 [f(f + \zeta) - M^2 s] \quad (15)$$

and the total energy change, $\Delta E = \Delta P + \Delta K$, is

$$\Delta E = \rho_0 \Delta y^2 \left[f(f + \zeta) - M^2 s + N^2 s \left(s - \frac{M^2}{N^2} \right) \right]. \quad (16)$$

Factoring M^2 out of the bracketed expression in (15), one has

$$\Delta K = \rho_0 \Delta y^2 M^2 \left[\frac{f(f + \zeta)}{M^2} - s \right] \quad (17)$$

¹ A flow is unstable to inertial instability if $f \partial \mathcal{M} / \partial x < 0$. In baroclinic flow the inertial instability becomes known as symmetric instability, and this criterion generalizes to $f \partial \mathcal{M} / \partial x|_\rho < 0$, where the subscript ρ indicates that the derivative is evaluated along an isopycnal surface (Holton and Hakim, 2012).

revealing that there is no change in mean KE when parcels are exchanged along \mathcal{M} -surfaces. SI modes aligned with these surfaces thus grow purely via the extraction of background PE, forming a

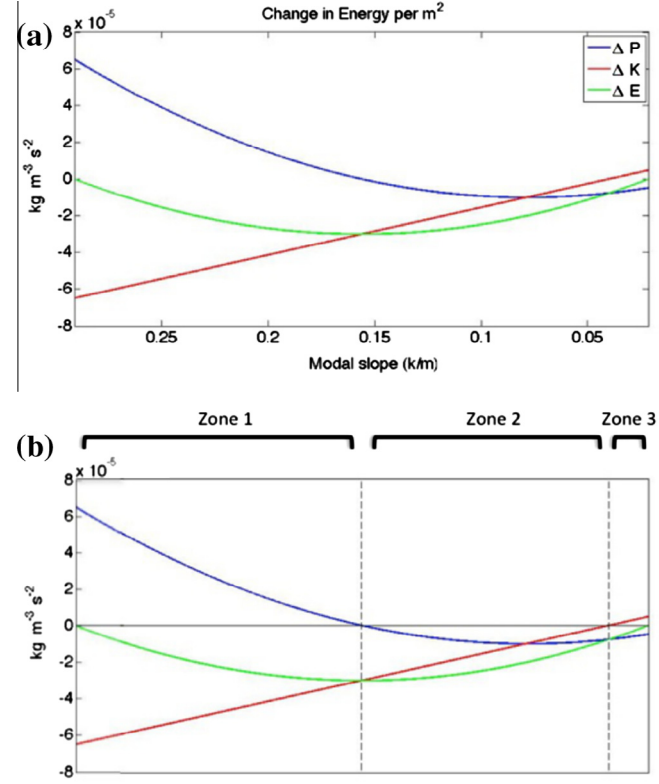


Fig. 1. (a) Change in total, kinetic, and potential energy per unit density per square meter for a parcel displacement Δy over all slopes unstable to SI. The parameters were set to be $f = 10^{-4} \text{ s}^{-1}$, $N^2 = 1.6 \times 10^{-6} \text{ s}^{-2}$, $M^2 = 2.5 \times 10^{-7} \text{ s}^{-2}$, $\partial v / \partial x = 0$, and $Ri = 0.25$. The change in total energy tends to zero at the edges of this “unstable arc”. (b) The SI obtains its energy differently depending on the angle k/m . In zone 1, the SI gains energy by reducing the geostrophic shear, but some of this gain is offset by conversion to mean PE. In zone 2, the SI gains energy both through reducing PE and through geostrophic shear production. In zone 3, SI reduces the mean PE but also contributes some energy to the background KE.

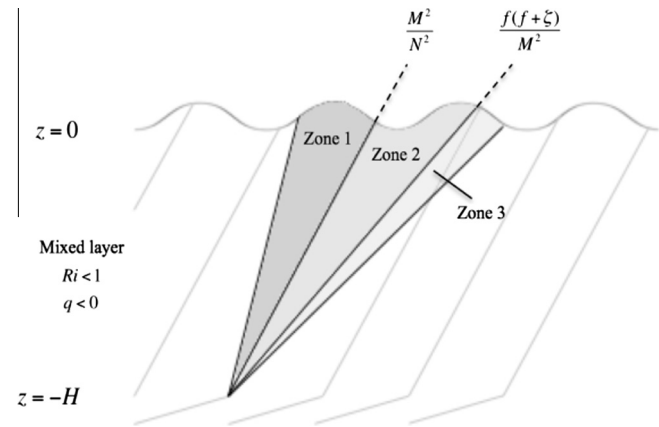


Fig. 2. Schematic of an idealized mixed layer showing SI-unstable zones. The mixed layer extends from $-H < z < 0$ and lies atop a highly stratified thermocline that is stable to SI. The SI modes extract energy from the background flow differently depending on which zone their slopes fall into. Isopycnals are shaded gray lines, and represent the boundary between zones 1 and 2. The absolute momentum contour represents the boundary between zones 2 and 3.

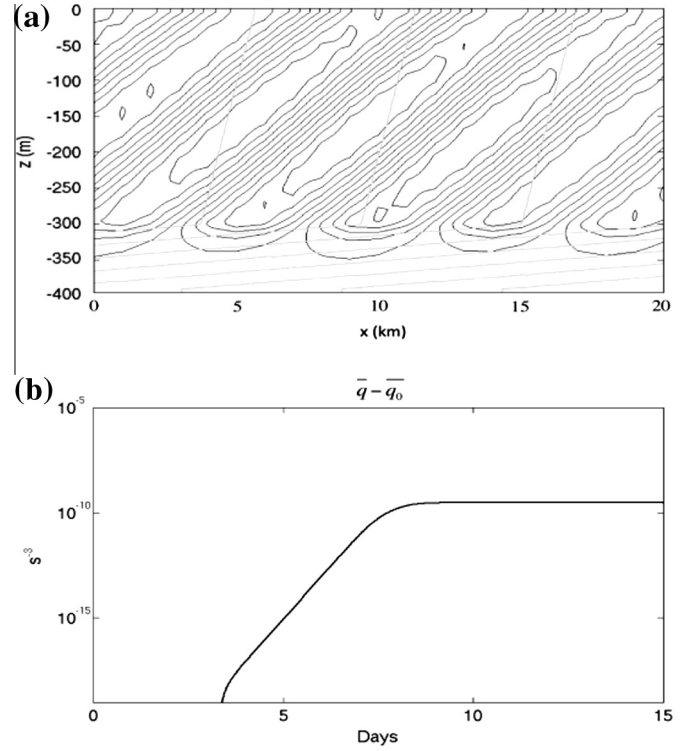


Fig. 3. (a) Isopycnals (gray) and contours of cross-frontal velocity (black), taken from a 20 km-wide section of simulation A_3 (Section 3) during the exponential growth phase at $t = 5$ days. The boundary between the mixed layer and thermocline occurs at $z = -300$ m. Though only the mixed layer is unstable to SI, the SI overturning cells penetrate into the thermocline, entraining highly stratified, high-PV fluid. This fluid is then rapidly mixed upwards, increasing the stratification and mean PV of the mixed layer. (b) Change in mean PV of the mixed layer over the course of the simulation. The change prior to $t \approx 4$ days is not shown because it is smaller than the machine precision.

dichotomy with isopycnal-aligned modes, which grow purely via reduction of the geostrophic shear.

One can extend this analysis to consider modes whose slope is between or around the isopycnals and \mathcal{M} -surfaces as well. Substituting (9) into (16) reveals that $\Delta E = 0$ at the edges of the unstable arc; furthermore, Fig. 1 reveals that the extraction of energy smoothly transitions to zero as the edges are approached. Three “zones” thus exist: zone 1 contains all modes whose slope is steeper than the isopycnal, which grow by reducing the geostrophic shear but convert some of the extracted KE to mean PE in the background stratification; zone 2 lies between the isopycnal and the \mathcal{M} -surface, where both the background PE and KE are reduced; zone 3 lies between the \mathcal{M} -surface and the shallowest unstable slope, where the background PE is reduced but some KE is transferred back into the mean flow. A schematic of these zones appears in Fig. 2.

2.3. Restratification by SI in models

The energetics of the unstable SI modes reveal that restratification is indeed possible in the absence of secondary Kelvin–Helmholtz instabilities. Here restratification is defined as an increase in bulk Ri , which can be achieved by either an increase in N^2 , a decrease in M^4 , or even a decrease in N^2 which is offset by a larger decrease in M^4 . This definition differs from the usual meaning of restratification that $\partial N^2 / \partial t > 0$, but is required because as SI acts to restore to zero PV (so that $\partial q / \partial t > 0$) it adjusts the horizontal as well as vertical stratification so that $\partial Ri / \partial t > 0$. This restratification is induced by an extraction of mean KE or PE depending on which zone the mode occupies, which manifests as a tilting of iso-

pycnal surfaces toward the horizontal. The overall effect is a simultaneous decrease of both N^2 and M^2 in zone 1, an increase of N^2 and decrease of M^2 in zone 2, and an increase of both in zone 3. Though either of M^2 or N^2 can increase (decrease) during this process, the other decreases (increases) enough so that Ri increases in all cases, thereby restratifying the flow. However, a subtlety of this process is that in the absence of mixing the PV of the fluid is conserved. Thus, in an unbounded fluid where a source of higher-PV fluid is absent, the overall stability of the flow to SI is unchanged.

To change the stability of the flow to SI requires a source of higher-PV fluid. Now suppose a more realistic scenario, where a mixed layer unstable to SI overlies a thermocline whose higher stratification makes it stable to SI. In this case the SI overturning cells which grow from the released mean energy penetrate into the thermocline, entraining higher-PV fluid (Taylor and Ferrari, 2009) and increasing the mean PV in the mixed layer (Fig. 3). As the restratification and mixing continue the bulk Richardson number will increase until the flow becomes SI-neutral, whereupon

$$Ri_{q=0} = f/(f + \zeta). \quad (18)$$

The adjustment of the background flow by the SI modes allows one to consider what happens when model resolution is decreased and SI begins to be explicitly resolved. First consider an idealized simulation where Δz is fixed and uniform throughout the domain, and where Δx is chosen such that only modes in zone 3 (e.g. those with the shallowest slope) are resolved. As PE is released and the isopycnals slump toward the horizontal, more of the unstable arc becomes resolvable as the slope of the unstable modes decreases. Modes in zone 2 may then become resolved, which extract energy from both the vertical shear and the background PE. If the restratification persists to the point where the isopycnal slope itself is resolved, it is likely that the flow will fully restratify until (18) is reached.

However, this does not necessarily mean that a flow with unstable SI modes can always fully restratify. Despite the fact that the mean effect of SI will decrease the isopycnal slope, it does not decrease the slope of the shallowest mode. This can be seen by taking the slope of this mode, which was shown in (9) to be

$$S = \frac{k}{m} = \frac{M^2}{N^2} - \frac{f}{N} \sqrt{\frac{1}{Ri} - \left(1 + \frac{\zeta}{f}\right)} \quad (19)$$

and noting that $\partial S/\partial N > 0$. Therefore, as the flow restratifies the slope of this mode increases and the mode becomes unresolved if $S > H/\Delta x$, where H is the depth of the mixed layer. It is possible that, for the scenario above where only zone 3 modes are resolved at the outset, the shallowest modes will become unresolved before the isopycnal slope becomes resolved (i.e. $M^2/N^2 < H/\Delta x$), and the restratification will terminate at a stage when $Ri_{t=0} < Ri < f/(f + \zeta)$. The addition of viscosity complicates this scenario since it damps modes asymmetrically about the most unstable slope.

Ultimately, the rate at which the SI modes become resolvable or unresolvable is a nontrivial function of Ri , the relative vorticity, and the viscosity, and in general it is extremely difficult to predict what the ultimate stabilized state will be. In cases where the starting Ri is very small, the difference between the isopycnal slope and the shallowest unstable slope is very large (in fact, it can become infinite as $Ri \rightarrow 0$), meaning that even on coarse grids some restratification could occur. Granted, the growth rates of the modes in the very small Ri limit are very small as well, and it is likely that even in the absence of explicit viscosity/diffusion some numerical diffusion will restratify more quickly than the SI modes. Perhaps more importantly the flow will be unstable to KH instability, or a boundary layer parameterization such as KPP (Large et al., 1994) would become active.

3. Simulations

Since SI is faster than many processes that are commonly resolved in ocean models, when SI is active the mean-flow properties might be expected to remain close to the SI-neutral state where $q = 0$ and $Ri = f/(f + \zeta)$. However, when SI is only partially resolved, the neutral state when $\sigma = 0$ may not necessarily correspond to $q = 0$. In this section the properties of the neutral state for partially-resolved SI will be examined. This will help to diagnose the effects of resolved and unresolved SI in ocean models.

Partial resolution of SI can be achieved by varying the viscosity and horizontal grid spacing, the two main controllers over how fully SI can restratify the mixed layer. This is best demonstrated using a set of simplified, idealized models where many of the flow parameters can be taken as constant. Though the linear theory of Appendix A is employed here to predict how much restratification takes place, it must be emphasized that the goal here is not to develop a parameterization for partially-resolved SI in GCMs. Rather, the models here serve to demonstrate that even in a highly simplified setting a combination of viscosity and gridscale effects can influence SI restratification, yielding a stable state not satisfying (18).

A suite of idealized models has been set up using an incompressible, nonhydrostatic, Boussinesq Navier–Stokes solver, the details of which can be found in Taylor (2008) and Bewley (2010). An important advantage of this model is that it is pseudo-spectral in the horizontal directions. Since the horizontal numerical viscosity and diffusivity are extremely small in these simulations, this allows the effects of the explicit model viscosity, diffusivity, and grid resolution to be isolated.

Since SI can grow independent of the along-front direction (see Appendix A) and the goal here is not to model baroclinic mixed layer instability as in Boccaletti et al. (2007) or Fox-Kemper et al. (2008), it is sufficient to run the simulations in 2D, as in previous studies (e.g. Thorpe and Rotunno, 1989, Griffiths, 2003, Taylor and Ferrari, 2009). Thus the models are run as 2D cross-channel spindown simulations of a symmetrically unstable front. Akin to Taylor and Ferrari, 2009, the initial state consists of a weakly stratified surface layer from $-300 \text{ m} < z < 0$ lying atop a more strongly stratified “thermocline” from $-400 \text{ m} < z < -300 \text{ m}$. A constant background M^2 is used for both the surface layer and the thermocline. The horizontal boundary conditions are set up in a “frontal zone” configuration; that is, the density and velocity fields are decomposed into departures from a constant background state defined by

$$b_T(x, z, t) = M^2 x + b(x, z, t), \quad (20)$$

$$\mathbf{u}_T(x, z, t) = V_G(z)\mathbf{j} + \mathbf{u}(x, z, t), \quad (21)$$

$$\frac{dV_G}{dz} = \frac{M^2}{f}, \quad (22)$$

where the subscript T indicates the total field. The model is set up to be horizontally periodic in the perturbation variables (no subscript), while the background state is assumed to be constant in time. The use of periodic boundary conditions allows the flow to freely evolve with no influence from lateral boundaries and no need to specify inflow/outflow conditions. The upper boundary is adiabatic with a rigid lid, and both vertical boundaries are set to be free-slip on the perturbation velocity \mathbf{u} . Throughout the rest of this paper this model setup will be referred to as “frontal zone”. Finally, the initial density field is perturbed by a white noise with an amplitude of $10^{-4} \text{ kg m}^{-3}$.

Four sets of simulations have been conducted in order to test the sensitivity of restratification by SI to different combinations of M^2 , N^2 , and v_h . The parameter choices for each set of simulations are listed in Table 1. The simulation parameters for each set are

chosen such that the initial Richardson number in the surface layer is 0.25, which is neutral to KH instability (Stone, 1966) but still unstable to SI. The Richardson number in the thermocline is set at 12.5 so that it is stable to both types of instability.

Each simulation set consists of seven individual simulations run at varying resolutions; individual simulations will henceforth be referred to by a numerical subscript (e.g. A_1, B_3 , etc.). The advantage of using a frontal zone 2D model is that f and the domain-averaged M^2 are constant in time, so that the time evolution of Ri is governed only by the change in N^2 . Then the linear growth rates for viscous hydrostatic and nonhydrostatic SI, which are

$$\sigma = \left[\frac{M^4}{N^2} - (f^2 + f\zeta) - N^2 \left(\frac{k}{m} - \frac{M^2}{N^2} \right)^2 \right]^{1/2} - (v_h k^2 + v_v m^2) \quad (23)$$

and

$$\sigma = \left[\frac{M^4}{N^2} - (f^2 + f\zeta) - N^2 \left(\frac{k}{m} - \frac{M^2}{N^2} \right)^2 \right]^{1/2} \left(1 + \frac{k^2}{m^2} \right)^{-1/2} - (v_h k^2 + v_v m^2), \quad (24)$$

respectively, can be used to predict the restratification potential of the SI modes. That is, using $\zeta = 0$, setting k and m according to the grid spacing and holding M^2, f, v_h , and v_v constant, the growth rates can be plotted purely as a function of N^2 . Furthermore, beginning with an initial state where $Ri = 0.25$, it is known *a priori* that N^2 must increase by a factor of 4 to reach the stable state of $Ri = 1$. Then the growth rates can be calculated for a discrete set of values of N^2 between N_0^2 and $4N_0^2$ to predict the SI-stable value of N^2 that will be reached, and by extension the stable value of Ri . Note that (23) and (24) require both M^2 and N^2 to be constant in space and time and the perturbations to be small in amplitude, and are approximations to the instantaneous growth rate found by holding N^2 fixed at each instant in time.

The grid spacing Δx is varied from simulation to simulation to test the hypothesis that the amount of restratification depends on how well the SI modes are resolved. The pseudo-spectral numerical solver uses a Two-Thirds Rule de-aliasing (Orszag, 1971) to prevent aliasing of high-wavenumber modes, making the shortest resolved wavelength in the model $\lambda = 3\Delta x$. The higher-resolution simulations (subscripts 1 through 5) are meant to demonstrate that the restratification can be limited by the stratification and viscosity, not necessarily the model resolution. The lowest-resolution simulations do not resolve the most-restratifying mode, and demonstrate restratification that is limited (subscript 6) and completely negated (subscript 7) due to the model resolution. The dimensional width of the domain varies according to the choice of Δx for each individual simulation, but the depth of the mixed layer is set to be 300 m in all cases. A uniform grid of size $(N_y, N_z) = (128, 80)$ points is used, with the vertical grid spacing set to a constant $\Delta z = 5$ m. Using this number of points in the horizontal ensures that the domain is wide enough to resolve multiple SI overturning cells in all cases, and that the largest SI modes will not be excluded even in the finest-resolution runs.

The vertical diffusivity $\kappa_v = 1 \times 10^{-6} \text{ m}^2 \text{ s}^{-1}$ was set to be very small to prevent highly stratified fluid from diffusing up from the thermocline, and for simplicity in the stability analysis (Appendix A) the vertical viscosity was set to match this value. At higher values (i.e. $\kappa_v \geq 1 \times 10^{-4} \text{ m}^2 \text{ s}^{-1}$), diffusion caused the lowest parts of the mixed layer to become stabilized to SI before the instability became nonlinear. This effectively reduced the lengthscale of the gravest vertical mode and reduced the amount of restratification that could occur. It was also difficult to quantify the effective value

of m by the time the SI modes became nonlinear with this larger diffusivity. Using the simulation parameters in Table 1, the linear stability analysis was insensitive to setting v_v to this smaller value, so for the purpose of this modeling exercise the smaller viscosity/diffusivity sufficed.

3.1. Hydrostatic and nonhydrostatic models

One consequence of varying N^2 and M^2 is that the dynamics may become sensitive to whether the hydrostatic approximation is employed. Because the balanced Richardson number can be tuned by adjusting the values of M^2, N^2 , and f , the individual parameters for each set are chosen to fix the hydrostatic parameter (Marshall et al., 1997)

$$\eta = \frac{\gamma^2}{Ri}, \quad (25)$$

where $\gamma = h/L$ is the aspect ratio of the motion. For $\eta \ll 1$ it is appropriate to use the hydrostatic approximation to the vertical momentum equation.

The parameter γ is estimated according to the initial M^2 and N^2 from the simulations. Because the unstable modes lie in an arc symmetric about the isopycnal, the mean aspect ratio of the motions can be taken as $\gamma = M^2/N^2$, and simple algebra gives

$$\eta = \frac{f^2}{N^2} \frac{1}{Ri^2}. \quad (26)$$

The parameter choices in Table 1 are chosen so that $\eta = 0.1$ for the “hydrostatic” parameters and $\eta = 10$ for the “nonhydrostatic” parameters. Note that in both cases, the fully nonhydrostatic equations are solved. To check whether the results are sensitive to whether a model is run in hydrostatic mode, a parallel set of the $\eta = 0.1$ simulations was run using the MITgcm (Marshall et al., 1997) in hydrostatic mode and with identical initial conditions. The hydrostatic MITgcm gave nearly identical results (not shown) as long as the grid spacing Δx was less than half the wavelength of the most unstable mode; when Δx was set above this threshold the MITgcm was prone to numerical instability which eventually led to the simulation crashing. This numerical instability influenced the choice to use the nonhydrostatic solver for these simulations over the MITgcm. Nonetheless, previous work by Mahadevan (2006) suggests that the average vertical fluxes at the length scales in these simulations should be similar regardless of whether the model is run hydrostatically or nonhydrostatically, so it is likely that the results from the nonhydrostatic solver are robust for the $\eta = 0.1$ simulations at all resolutions.

The simulation parameters in Table 1 were chosen specifically to demonstrate cases of grid-arrested restratification (Sets A and C) and completed restratification (B and D) by varying v_h . The amount of restratification that takes place is not uniquely dependent on the parameter choices in each set; all of the parameters can be varied in relation to one another to change the anticipated final value of Ri . Fig. 4 shows the growth rate plots for each parameter set. In each case the horizontal viscosity damps the highest wavenumber modes, so that increasing the resolution beyond a certain point does not permit extra modes to become resolved or further restratification to occur. The growth rates are calculated by fixing the vertical wavenumber $m = 2\pi/H$, corresponding to a wavelength equal to the depth of the mixed layer. Setting m in this way guarantees the plotted growth rates are for those modes least affected by viscous damping since it is the smallest vertical wavenumber allowed in the mixed layer. Furthermore, for any wavenumber k the modes with minimal m will have the largest slope. Therefore, in a scenario such as (19) where the slope of the unstable modes becomes greater than the maximum resolvable

Table 1

Parameters for the hydrostatic and nonhydrostatic simulations. A subscript *S* denotes a property of the surface layer, and *T* refers to a property of the thermocline. Seven simulations were conducted per set at different horizontal resolutions Δx . The shortest resolved wavelength due to the Two-Thirds filter is equal to $3\Delta x$. The bulk Richardson number of each simulation when the model becomes SI-neutral is $Ri_{t=\infty}$, and can be compared with the prediction from linear theory Ri_L when all modes are resolved. Individual simulations are referred to by their set label (A through D) and a numerical subscript.

HYDROSTATIC					
$N_S^2 = 1.6 \times 10^{-6} \text{ s}^{-2}$ $N_T^2 = 8 \times 10^{-5} \text{ s}^{-2}$ $M^2 = 2.5 \times 10^{-7} \text{ s}^{-2}$ $f = 10^{-4} \text{ s}^{-1}$					
$\nu_\nu = \kappa_\nu = 10^{-6} \text{ m}^2 \text{ s}^{-1}$ $\eta = 0.1$ $H = 300 \text{ m}$					
SET A: $\nu_h = \kappa_h = 80 \text{ m}^2 \text{ s}^{-1}; Ri_L = 0.76$			SET B: $\nu_h = \kappa_h = 10 \text{ m}^2 \text{ s}^{-1}; Ri_L = 1.00$		
A_1 :	$\Delta x = 250 \text{ m}$	$Ri_{t=\infty} = 0.71$	B_1 :	$\Delta x = 250 \text{ m}$	$Ri_{t=\infty} = 1.12$
A_2 :	$\Delta x = 500 \text{ m}$	$Ri_{t=\infty} = 0.79$	B_2 :	$\Delta x = 500 \text{ m}$	$Ri_{t=\infty} = 1.08$
A_3 :	$\Delta x = 1000 \text{ m}$	$Ri_{t=\infty} = 0.77$	B_3 :	$\Delta x = 1000 \text{ m}$	$Ri_{t=\infty} = 1.06$
A_4 :	$\Delta x = 2000 \text{ m}$	$Ri_{t=\infty} = 0.77$	B_4 :	$\Delta x = 2000 \text{ m}$	$Ri_{t=\infty} = 1.23$
A_5 :	$\Delta x = 3000 \text{ m}$	$Ri_{t=\infty} = 0.77$	B_5 :	$\Delta x = 3000 \text{ m}$	$Ri_{t=\infty} = 1.37$
A_6 :	$\Delta x = 4000 \text{ m}$	$Ri_{t=\infty} = 0.56$	B_6 :	$\Delta x = 4000 \text{ m}$	$Ri_{t=\infty} = 1.37$
A_7 :	$\Delta x = 5000 \text{ m}$	$Ri_{t=\infty} = 0.25$	B_7 :	$\Delta x = 5000 \text{ m}$	$Ri_{t=\infty} = 0.25$
NONHYDROSTATIC					
$N_S^2 = 1.6 \times 10^{-8} \text{ s}^{-2}$ $N_T^2 = 8 \times 10^{-7} \text{ s}^{-2}$ $M^2 = 2.5 \times 10^{-8} \text{ s}^{-2}$ $f = 10^{-4} \text{ s}^{-1}$					
$\nu_\nu = \kappa_\nu = 10^{-6} \text{ m}^2 \text{ s}^{-1}$ $\eta = 10$ $H = 300 \text{ m}$					
SET C: $\nu_h = \kappa_h = 1 \text{ m}^2 \text{ s}^{-1}; Ri_L = 0.63$			SET D: $\nu_h = \kappa_h = 0.1 \text{ m}^2 \text{ s}^{-1}; Ri_L = 1.00$		
C_1 :	$\Delta x = 25 \text{ m}$	$Ri_{t=\infty} = 0.56$	D_1 :	$\Delta x = 25 \text{ m}$	$Ri_{t=\infty} = 1.17$
C_2 :	$\Delta x = 50 \text{ m}$	$Ri_{t=\infty} = 0.52$	D_2 :	$\Delta x = 50 \text{ m}$	$Ri_{t=\infty} = 1.20$
C_3 :	$\Delta x = 100 \text{ m}$	$Ri_{t=\infty} = 0.56$	D_3 :	$\Delta x = 100 \text{ m}$	$Ri_{t=\infty} = 1.17$
C_4 :	$\Delta x = 200 \text{ m}$	$Ri_{t=\infty} = 0.54$	D_4 :	$\Delta x = 200 \text{ m}$	$Ri_{t=\infty} = 1.26$
C_5 :	$\Delta x = 300 \text{ m}$	$Ri_{t=\infty} = 0.55$	D_5 :	$\Delta x = 300 \text{ m}$	$Ri_{t=\infty} = 1.35$
C_6 :	$\Delta x = 400 \text{ m}$	$Ri_{t=\infty} = 0.41$	D_6 :	$\Delta x = 400 \text{ m}$	$Ri_{t=\infty} = 1.35$
C_7 :	$\Delta x = 500 \text{ m}$	$Ri_{t=\infty} = 0.25$	D_7 :	$\Delta x = 500 \text{ m}$	$Ri_{t=\infty} = 0.25$

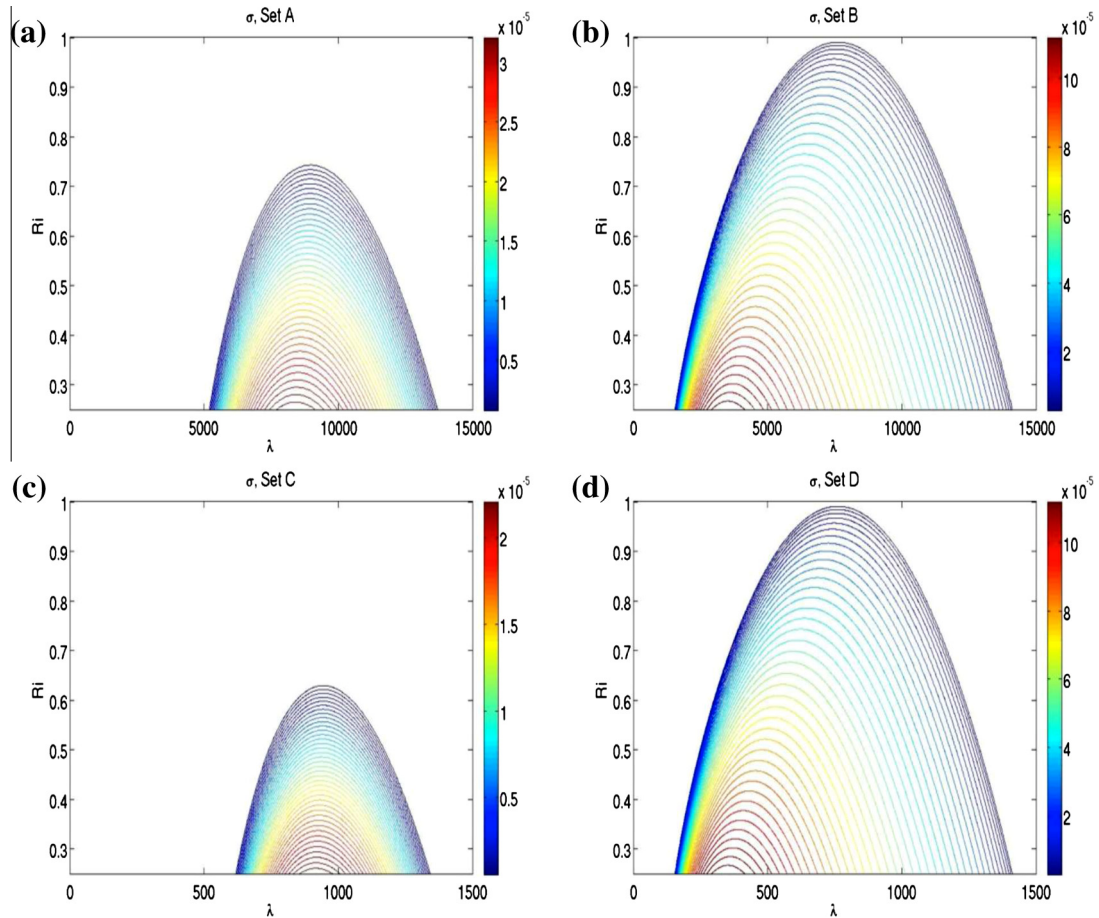


Fig. 4. Linear growth rate plots for each simulation set as a function of horizontal wavelength λ and balanced bulk Richardson number. The growth rate is calculated by taking M^2, f , and viscosity as in Table 1, and by letting $m = 2\pi/H$ be the vertical wavenumber. Plots (a) and (c) predict restratification will be arrested prior to achieving (18) no matter how small Δx is set. The restratification potential is further reduced when the most restratifying mode is not resolved, which in the simulations occurs when $\Delta x > 3000 \text{ m}$ and $\Delta x > 300 \text{ m}$, respectively. Plots (b) and (d) suggest that the simulation parameters will allow the fully restratified state to satisfy (18).

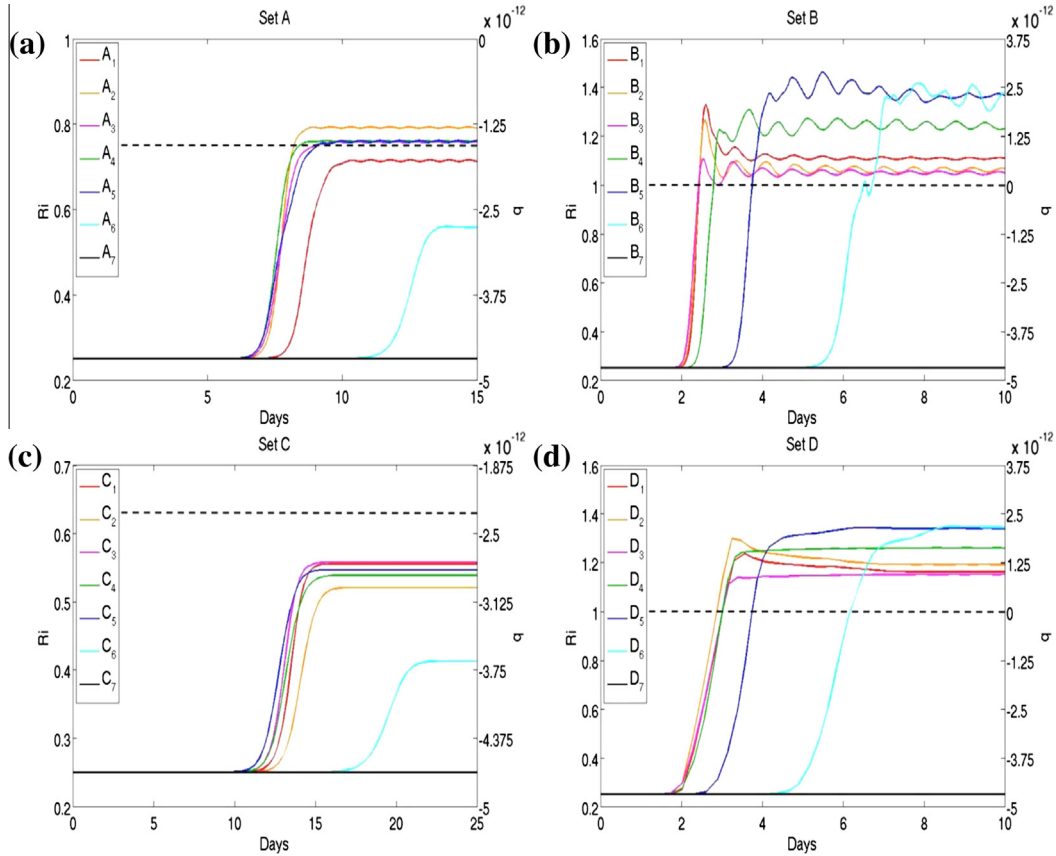


Fig. 5. Growth of mean Ri and q averaged over the depth range from -250 m to -50 m, along with their maximum values predicted by linear theory (dashed line). The restratification in Sets A and C is arrested by a combination of the horizontal viscosity and grid resolution, while the restratification in Sets B and D exceed the predicted value due to a numerical artifact of anisotropic viscosity (see Section 3.1.3). The resolution of simulation₇ from all sets is set so that no SI modes are resolved, and thus Ri and q remain at their initial values.

slope $H/\Delta x$, the modes with $m = 2\pi/H$ will be the last to be resolved. For these reasons taking the minimum m in Fig. 4 represents the maximum predicted restratification by SI.

Fig. 5 shows the evolution of the Richardson number and potential vorticity for each simulation set until all runs have become neutral to SI. The results are averaged in x and over all points in z from -250 m to -50 m depth so as to avoid contaminating the statistics with the surface boundary layer and with fluid diffused from the thermocline. Linear theory predicts an exponential growth of the unstable modes; after a few days the SI becomes nonlinear and leads to a rapid increase in Ri and q . The actual time before the increase in Ri and q depends on the growth rate of the fastest-growing mode, which in turn is a function of the flow parameters and the viscosity. When this mode is not resolved the growth rate depends on the fastest resolved mode, which can be substantially slower (simulations₆ in all sets).

The simulations reveal three possible outcomes:

3.1.1. Case I: restratification limited by viscosity

The first outcome is demonstrated in simulations A_{1-5} and C_{1-5} , where the steady-state Richardson number matches the value predicted by linear theory to within 5% and 16%, respectively. In these simulations the grid spacing is sufficiently fine to resolve the most-restratifying mode, so that restratification is incomplete only due to the horizontal viscosity. The incomplete restratification occurs for any grid spacing finer than the ones used here, since the horizontal viscosity damps out the modes that would restratify to the point where $Ri = 1$. The prediction for Set C performed slightly worse because the smaller viscosity allowed stronger overturning cells to form, which penetrated more deeply into the thermocline

(as in Fig. 3). High-PV fluid entrained by the overturning penetrated into the lowest part of the mixed layer and made it stable to SI, increasing the effective vertical wavenumber of the remaining SI modes. As an example of the effect this has on the prediction from Fig. 4, increasing the vertical wavenumber from $m = 2\pi/H \approx .0209$ to $m = 2\pi/(H - 10 \text{ m}) \approx .0217$ reduces the predicted Ri from 0.63 to 0.57 – using the latter value would make the results accurate to within 6%. This effect also occurred subtly in simulation A_1 due to the finer horizontal grid spacing, resulting in a steady Ri slightly less than the linear prediction.

3.1.2. Case II: restratification limited by resolution

The second outcome is demonstrated in simulations A_6 and C_6 , where the most restratifying mode is not resolved and restratification is arrested by a combination of the horizontal viscosity and the coarseness of the grid. The steady-state Richardson number can still be predicted by linear theory, however. Finding the predicted value amounts to moving right along the λ -axis in Fig. 4 to the point where $\lambda = 3\Delta x$. At this point, which corresponds to the grid cutoff scale, the maximal value of Ri with $\sigma > 0$ is the predicted restratification potential of the resolved SI modes. In simulation A_6 linear theory predicts the flow to become SI-neutral at $Ri \approx 0.56$, matching the simulated value to within 1%. The prediction for simulation C_6 again did not perform as well due to entrainment from the thermocline, yielding a steady $Ri \approx 0.41$ compared with a predicted value of $Ri \approx 0.47$.

This outcome represents the most likely scenario that would occur in an ocean model, where some combination of coarse grid spacing and viscosity would limit the presence of SI modes and thereby limit restratification of the mixed layer. Note, however,

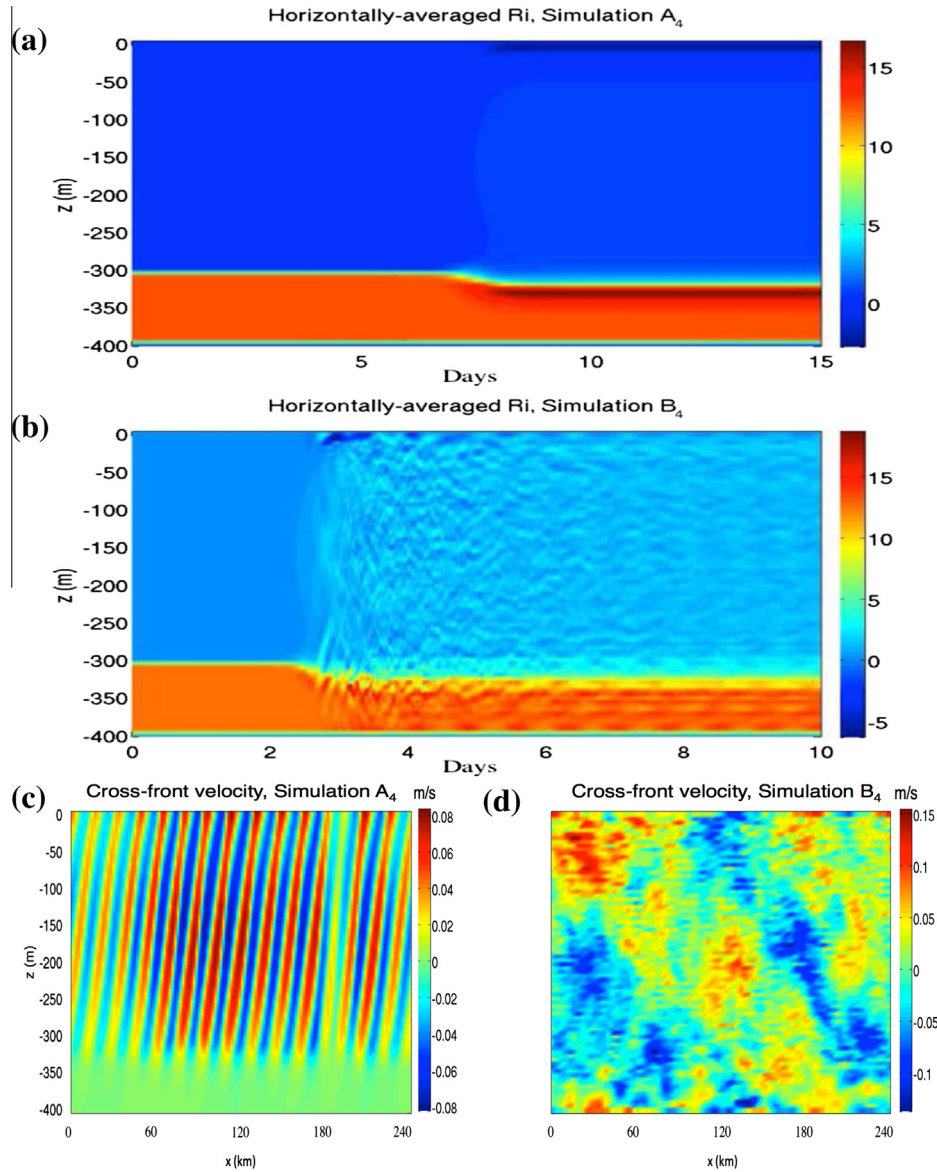


Fig. 6. Evolution of horizontally-averaged Ri over time from simulations (a) A_4 and (b) B_4 . Small-scale turbulence entrains high-PV fluid from the thermocline in both simulations. (c) Cross-front velocity at $t \approx 8$ days in A_4 compared with (d) the cross-front velocity at $t \approx 4$ days in B_4 . Both snapshots are taken shortly after the deepening of the thermocline and well into the nonlinear SI phase. Overturning cells in A_4 are well-organized and decay rapidly in the thermocline, while B_4 features a chaotic velocity field with gridscale noise. A numerical consequence of using anisotropic viscosity is that strong mixing occurs deep into the thermocline which should otherwise be stable to both Kelvin–Helmholtz and symmetric instabilities. The entrained fluid gets mixed upward rapidly, exciting strong inertial oscillations and resulting in a mixed layer average $Ri > 1$ and $q > 0$.

that in the general case of an ocean model where mixed layer depth, forcing, viscosity, and stratification are all varying in time and space the restratification potential will not be easily predictable. Nonetheless, the cases here demonstrate that the grid spacing can affect restratification by making some of the SI modes unresolvable.

3.1.3. Case III: excessive restratification due to anisotropic viscosity

The third outcome is perhaps the most interesting, and occurs when the horizontal and vertical viscosities are small enough to permit a full restratification by the SI modes but are anisotropic (Sets B and D). In finely-resolved simulations with isotropic viscosity and nearly-isotropic grid spacing secondary Kelvin–Helmholtz instabilities form in the shear zones between SI cells (Taylor and Ferrari, 2009), which serve to mix potential vorticity across density surfaces. Simulations with coarse horizontal resolution develop these shear zones between cells as well, but the anisotropic

viscosity does not permit fully realized shear instability to form at these locations.

The resulting flow features localized regions of vigorous, small-scale noise (Fig. 6(d)) that act as a nonphysical source of mixing, after which the steady-state flow is characterized by strong inertial oscillations with $Ri > 1$ and $q > 0$. This overturning penetrates deep into the thermocline and entrains a large amount of high-PV fluid, which is then rapidly mixed up into the interior of the mixed layer and causes the overshoot in Ri and q . Some entrainment is to be expected in all scenarios since the SI overturning cells extend into the thermocline (Fig. 3(a)), but in Sets B and D strong mixing occurs in the interior of the thermocline and persists even after the majority of the mixed layer restratification is complete, suggesting that this mechanism is nonphysical (Fig. 6(b) and (d)). The velocity fields in these simulations featured gridscale noise whose amplitude was strong even in the thermocline, where the higher stratification should have suppressed any physical instabilities. Gridscale noise

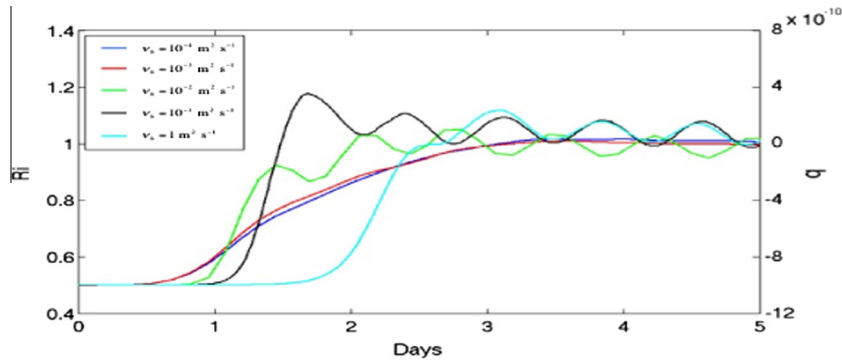


Fig. 7. Growth of mean Ri and q averaged over the depth range from -10 m to -40 m, for a mixed layer extending from $0 > z > -50$ m as in Taylor and Ferrari (2009). Linear theory predicts that the flow will become SI-neutral at $Ri = 1$ and $q = 0$ for all values of $v_h = \kappa_h$ used here. Though the growth rates are slower for the more viscous simulations and the onset of the nonlinear phase comes later, the restratification after this point occurs more quickly. Excessive restratification occurs as the viscosity and diffusivity become more anisotropic ($v_v = \kappa_v = 10^{-4} \text{ m}^2 \text{ s}^{-1}$), though the grid aspect ratio $\Delta z/\Delta x = 1$ in all cases.

in regions where the flow should be relatively quiescent might be an indicator of this type of instability; further testing in other GCMs is necessary to check whether this is true.

The unphysical mixing effect occurred in both the nonhydrostatic solver and the MITgcm, and as such the authors consider it a general numerical issue that may arise when using anisotropic viscosity. To explore further, another set of five simulations was run with an isotropic grid ($\Delta x = \Delta z = 1$ m) and stratification parameters as in Taylor and Ferrari (2009), except that the horizontal viscosity and diffusivity were set to $v_h = \kappa_h = \{10^{-4}, 10^{-3}, 10^{-2}, 10^{-1}, 1\} \text{ m}^2 \text{ s}^{-1}$. This configuration was chosen because in their original paper Taylor and Ferrari (2009) used isotropic viscosity and diffusivity with $v_h = \kappa_h = 10^{-4} \text{ m}^2 \text{ s}^{-1}$ on an isotropic grid, and obtained full restratification to $q = 0$ and $Ri = 1$. The linear stability calculator predicts that full restratification would also be achieved for any choice of v_h in the set above. Therefore, if the vertical viscosity is held fixed at $v_v = 10^{-4} \text{ m}^2 \text{ s}^{-1}$ and the horizontal viscosity is increased, any overshoot in either Ri or q can be attributed to anisotropic viscosity.

Indeed, Fig. 7 demonstrates a progressively larger overshoot in both Ri and q , as well as more energetic inertial oscillations, as v_h is increased away from $v_v = 10^{-4} \text{ m}^2 \text{ s}^{-1}$. These results suggest that the use of anisotropic viscosity is at least partly responsible for the excessive restratification, though this effect does seem to be amplified as the grid aspect ratio $\Delta z/\Delta x$ becomes smaller (Fig. 5(b)). The converse scenario (isotropic viscosity and anisotropic grid) was not tested due to the prohibitively small timestep it would require – in order to permit SI the vertical viscosity (and thus horizontal viscosity) must be kept very small, which makes modelling of this situation prohibitively expensive.

As the stratification of the mixed layer plays a key role in communicating atmospheric forcing to the interior of the ocean, excessive or improperly represented restratification could negatively impact climate prediction on long time scales. Further investigation of this numerical issue is beyond the scope of this paper. To the authors' knowledge this effect has not been previously documented, but due to the ubiquity of using anisotropic viscosity in GCMs it is possible that this it would occur in non-SI flow regimes as well.

4. Conclusion

In this paper a set of 2D numerical simulations have been conducted to demonstrate how a combination of model viscosity and grid resolution can affect mixed layer restratification by symmetric instability. Linear theory is used to predict the growth and restratification potential of SI modes resolved in the model. By varying the initial conditions and grid spacing, three possible scenarios are found that might occur when SI is partially resolved.

The first scenario is a case where the horizontal resolution is fine enough to resolve all of the SI modes necessary to restratify the mixed layer to a marginally stable state ($Ri = 1$ and $q = 0$), but where the horizontal viscosity is large enough to damp out some of the modes needed to reach this state. The end result is that the model equilibrates at a state that is unstable to SI ($Ri < 1$ and $q < 0$). The second scenario is similar to the first but where the model resolution is coarse enough that some of the SI modes are unresolved. Linear theory predicts that this case would occur when the grid spacing is too coarse to resolve the most-restratifying mode. Finally, the third scenario features an unphysical numerical instability that arises when $v_v \neq v_h$. In this case the flow becomes too stratified ($Ri > 1$ and $q > 0$) as a result of numerical artifacts. This occurs even when the grid resolution is sufficient to directly resolve the shear instability, and so is attributed here to the use of anisotropic viscosity. It is likely that this effect is not isolated to the flow scenarios depicted here, for which further investigation may be warranted.

It is important to note that the scenarios above are not necessarily tied to the explicit model viscosity; that is, the numerical viscosity can just as easily affect SI restratification in cases where it dominates the model viscosity. Given that the relationship between the numerical viscosity and model viscosity is affected by the choice of advection scheme, these scenarios could occur in idealized models or models running with extremely low model viscosity as well as larger-scale GCMs. Inclusion of other parameterizations such as KPP (Large et al., 1994) or viscous closures would also strongly affect the SI dynamics in the model, as they could induce large mixed layer viscosities that could quash the growth of SI modes.

It is of interest to submesoscale modelers to know at what resolution SI begins to become resolved at the gridscale, and what effect it would have upon the mixed layer stratification once it becomes present. Fig. 4 demonstrates that the linear growth rate can be used to predict the wavelength of the largest SI modes when the mixed layer N^2 and M^2 are uniform and slowly varying in time. A prediction made in this way would require knowledge of the model viscosity and diffusivity, and would be improved by accounting for contributions to each of these by other parameterizations such as KPP. For a more dynamically evolving mixed layer the simple, if unsatisfying, answer is that the necessary resolution depends heavily on the local flow parameters. Factors that would make a true resolution-dependent prediction of SI more difficult include (but are not limited to) the high variability of the buoyancy frequencies and unstable layer depth in the mixed layer, the common use of flow-dependent viscosity parameterizations (e.g., Smagorinsky, 1963, 1993), and the influence of other stratification-sensitive parameterizations.

In the future GCM resolution will become sufficiently fine to resolve larger-scale (e.g. mesoscale baroclinic) instabilities, but it will still be necessary to parameterize processes that occur at and below submesoscale resolution. Indeed, climate-scale models have a need for such parameterizations now. The results of this paper suggest that any attempted parameterization for symmetric instability should be able to modulate the mixed layer stratification so as to “pick up” the restratification process when the resolved modes are unable to proceed further. Two specific states to check for would be where locally $Ri < f/(f + \zeta)$, $q < 0$, or both, as these conditions would occur when SI is fully unresolved or partially resolved. Such a parameterization should also be self-tuning so as to avoid the issue of “double-counting” (e.g., [Delworth et al., 2012](#)), where the large modes are both resolved and parameterized. These issues are beyond the scope of this paper, but the results shown here may help in the construction and testing of a parameterization in the future.

Acknowledgements

The authors gratefully acknowledge support from the Natural Environment Research Council, award NE/J010472/1. We would like to thank two anonymous reviewers, whose comments and insight greatly helped to improve this work.

Appendix A. Linear stability analysis of nonhydrostatic, viscous SI

Begin with the primitive equations with anisotropic viscosity, and assume the flow is homogeneous in y , so that $\partial/\partial y = 0$. Then the governing equation set is

$$\frac{Du}{Dt} - fv + \frac{1}{\rho_0} \frac{\partial p}{\partial x} - v_h \frac{\partial^2 u}{\partial x^2} - v_v \frac{\partial^2 u}{\partial z^2} = 0, \quad (\text{A.1})$$

$$\frac{Dv}{Dt} + fu - v_h \frac{\partial^2 v}{\partial x^2} - v_v \frac{\partial^2 v}{\partial z^2} = 0, \quad (\text{A.2})$$

$$\beta \frac{Dw}{Dt} + \frac{g}{\rho_0} \rho + \frac{1}{\rho_0} \frac{\partial p}{\partial z} - \beta v_h \frac{\partial^2 w}{\partial x^2} - \beta v_v \frac{\partial^2 w}{\partial z^2} = 0, \quad (\text{A.3})$$

$$\frac{\partial u}{\partial x} + \frac{\partial w}{\partial z} = 0, \quad (\text{A.4})$$

$$\frac{D\rho}{Dt} - \kappa_h \frac{\partial^2 \rho}{\partial x^2} - \kappa_v \frac{\partial^2 \rho}{\partial z^2} = 0, \quad (\text{A.5})$$

where β is the “hydrostatic parameter” ($\beta = 0$ for hydrostatic flow, and $\beta = 1$ for non-hydrostatic). Consider a basic flow with

$$\rho = \rho_B(x) + \bar{\rho}(z) + \rho'(x, z), \quad (\text{A.6})$$

$$\mathbf{u} = V_G(z)\mathbf{j} + V_B(x)\mathbf{j} + \mathbf{u}'(x, z), \quad (\text{A.7})$$

where the prime variables are asymptotically small perturbations independent of y . Here the thermal wind velocity V_G is in balance with the mean buoyancy field, with V_B a barotropic velocity that varies over large lengthscales compared to \mathbf{u}' . Using the smallness of the perturbations to eliminate the nonlinear advection terms in (A.1)–(A.5), the perturbation equations are

$$\frac{\partial u'}{\partial t} - fv' + \frac{1}{\rho_0} \frac{\partial p'}{\partial x} - v_h \frac{\partial^2 u'}{\partial x^2} - v_v \frac{\partial^2 u'}{\partial z^2} = 0, \quad (\text{A.8})$$

$$\frac{\partial v'}{\partial t} + u' \frac{dV_B}{dx} + w' \frac{dV_G}{dz} + fu' - v_h \frac{\partial^2 v'}{\partial x^2} - v_v \frac{\partial^2 v'}{\partial z^2} = 0, \quad (\text{A.9})$$

$$\beta \frac{\partial w'}{\partial t} + \frac{g}{\rho_0} \rho' + \frac{1}{\rho_0} \frac{\partial p'}{\partial z} - \beta v_h \frac{\partial^2 w'}{\partial x^2} - \beta v_v \frac{\partial^2 w'}{\partial z^2} = 0, \quad (\text{A.10})$$

$$\frac{\partial u'}{\partial x} + \frac{\partial w'}{\partial z} = 0, \quad (\text{A.11})$$

$$\frac{\partial \rho'}{\partial t} + u' \frac{d\rho_B}{dx} + w' \frac{d\bar{\rho}}{dz} - \kappa_h \frac{\partial^2 \rho'}{\partial x^2} - \kappa_v \frac{\partial^2 \rho'}{\partial z^2} = 0. \quad (\text{A.12})$$

For easier notation, the differential operators on the left hand side will be grouped like so:

$$\left(\frac{\partial}{\partial t} - v_h \frac{\partial^2}{\partial x^2} - v_v \frac{\partial^2}{\partial z^2} \right) u' = f v' - \frac{1}{\rho_0} \frac{\partial p'}{\partial x}, \quad (\text{A.13})$$

$$\left(\frac{\partial}{\partial t} - v_h \frac{\partial^2}{\partial x^2} - v_v \frac{\partial^2}{\partial z^2} \right) v' = -u' \frac{dV_B}{dx} - f u' - w' \frac{dV_G}{dz}, \quad (\text{A.14})$$

$$\beta \left(\frac{\partial}{\partial t} - v_h \frac{\partial^2}{\partial x^2} - v_v \frac{\partial^2}{\partial z^2} \right) w' = -\frac{g}{\rho_0} \rho' - \frac{1}{\rho_0} \frac{\partial p'}{\partial z} = 0, \quad (\text{A.15})$$

$$\frac{\partial u'}{\partial x} = -\frac{\partial w'}{\partial z}, \quad (\text{A.16})$$

$$\left(\frac{\partial}{\partial t} - \kappa_h \frac{\partial^2}{\partial x^2} - \kappa_v \frac{\partial^2}{\partial z^2} \right) \rho' = -u' \frac{d\rho_B}{dx} - w' \frac{d\bar{\rho}}{dz} \quad (\text{A.17})$$

and the horizontal shear will be written in terms of the relative vorticity by substituting $V_B/\bar{x} = \zeta$. The first step is to take $(\partial/\partial t - \kappa_h \partial^2/\partial x^2 - \kappa_v \partial^2/\partial z^2)$ of (A.15) and substitute in (A.17):

$$\begin{aligned} \beta \left(\frac{\partial}{\partial t} - v_h \frac{\partial^2}{\partial x^2} - v_v \frac{\partial^2}{\partial z^2} \right) \left(\frac{\partial}{\partial t} - \kappa_h \frac{\partial^2}{\partial x^2} - \kappa_v \frac{\partial^2}{\partial z^2} \right) w' \\ = -\frac{1}{\rho_0} \left(\frac{\partial}{\partial t} - \kappa_h \frac{\partial^2}{\partial x^2} - \kappa_v \frac{\partial^2}{\partial z^2} \right) \frac{\partial p'}{\partial z} \\ - \frac{g}{\rho_0} \left(-u' \frac{d\rho_B}{dx} - w' \frac{d\bar{\rho}}{dz} \right). \end{aligned} \quad (\text{A.18})$$

Define the basic flow frequencies

$$M^2 \equiv -\frac{g}{\rho_0} \frac{d\rho_B}{dx} \quad N^2 \equiv -\frac{g}{\rho_0} \frac{d\bar{\rho}}{dz}. \quad (\text{A.19})$$

M^2 does not necessarily have to be constant, but for V_B to satisfy thermal wind balance M^2 must also vary over long lengthscales compared to \mathbf{u}' . Now taking $\partial^2/\partial x \partial z$ of (A.18), one has

$$\begin{aligned} \beta \left(\frac{\partial}{\partial t} - v_h \frac{\partial^2}{\partial x^2} - v_v \frac{\partial^2}{\partial z^2} \right) \left(\frac{\partial}{\partial t} - \kappa_h \frac{\partial^2}{\partial x^2} - \kappa_v \frac{\partial^2}{\partial z^2} \right) \frac{\partial^2 w'}{\partial x \partial z} \\ = -\frac{1}{\rho_0} \left(\frac{\partial}{\partial t} - \kappa_h \frac{\partial^2}{\partial x^2} - \kappa_v \frac{\partial^2}{\partial z^2} \right) \frac{\partial^3 p'}{\partial x \partial z^2} - M^2 \frac{\partial^2 u'}{\partial x \partial z} + N^2 \frac{\partial^2 w'}{\partial x \partial z}. \end{aligned} \quad (\text{A.20})$$

Now use the continuity equation (A.16) to substitute

$$\frac{\partial u'}{\partial x} = -\frac{\partial w'}{\partial z} \quad (\text{A.21})$$

giving

$$\begin{aligned} -\beta \left(\frac{\partial}{\partial t} - v_h \frac{\partial^2}{\partial x^2} - v_v \frac{\partial^2}{\partial z^2} \right) \left(\frac{\partial}{\partial t} - \kappa_h \frac{\partial^2}{\partial x^2} - \kappa_v \frac{\partial^2}{\partial z^2} \right) \frac{\partial^2 u'}{\partial x^2} \\ = -\frac{1}{\rho_0} \left(\frac{\partial}{\partial t} - \kappa_h \frac{\partial^2}{\partial x^2} - \kappa_v \frac{\partial^2}{\partial z^2} \right) \frac{\partial^3 p'}{\partial x \partial z^2} - M^2 \frac{\partial^2 u'}{\partial x \partial z} + N^2 \frac{\partial^2 u'}{\partial x^2}. \end{aligned} \quad (\text{A.22})$$

Now all terms are functions of u' except for one pressure term. To eliminate this term, take $\partial^2/\partial z^2$ of (A.13):

$$\left(\frac{\partial}{\partial t} - v_h \frac{\partial^2}{\partial x^2} - v_v \frac{\partial^2}{\partial z^2} \right) \frac{\partial^2 u'}{\partial z^2} = f \frac{\partial^2 v'}{\partial z^2} - \frac{1}{\rho_0} \frac{\partial^3 p'}{\partial x \partial z^2}. \quad (\text{A.23})$$

Now take $(\partial/\partial t - \kappa_h \partial^2/\partial x^2 - \kappa_v \partial^2/\partial z^2)$ of (A.23), giving

$$\begin{aligned} \left(\frac{\partial}{\partial t} - v_h \frac{\partial^2}{\partial x^2} - v_v \frac{\partial^2}{\partial z^2} \right) \left(\frac{\partial}{\partial t} - \kappa_h \frac{\partial^2}{\partial x^2} - \kappa_v \frac{\partial^2}{\partial z^2} \right) \frac{\partial^2 u'}{\partial z^2} \\ = f \left(\frac{\partial}{\partial t} - \kappa_h \frac{\partial^2}{\partial x^2} - \kappa_v \frac{\partial^2}{\partial z^2} \right) \frac{\partial^2 v'}{\partial z^2} \\ - \frac{1}{\rho_0} \left(\frac{\partial}{\partial t} - \kappa_h \frac{\partial^2}{\partial x^2} - \kappa_v \frac{\partial^2}{\partial z^2} \right) \frac{\partial^3 p'}{\partial x \partial z^2}. \end{aligned} \quad (\text{A.24})$$

It is now possible to substitute in for the pressure term in (A.22). This now becomes

$$\begin{aligned} & \left(\frac{\partial}{\partial t} - v_h \frac{\partial^2}{\partial x^2} - v_v \frac{\partial^2}{\partial z^2} \right) \left(\frac{\partial}{\partial t} - \kappa_h \frac{\partial^2}{\partial x^2} - \kappa_v \frac{\partial^2}{\partial z^2} \right) \frac{\partial^2 u'}{\partial z^2} \\ &= -\beta \left(\frac{\partial}{\partial t} - v_h \frac{\partial^2}{\partial x^2} - v_v \frac{\partial^2}{\partial z^2} \right) \left(\frac{\partial}{\partial t} - \kappa_h \frac{\partial^2}{\partial x^2} - \kappa_v \frac{\partial^2}{\partial z^2} \right) \frac{\partial^2 u'}{\partial x^2} \\ &+ f \left(\frac{\partial}{\partial t} - \kappa_h \frac{\partial^2}{\partial x^2} - \kappa_v \frac{\partial^2}{\partial z^2} \right) \frac{\partial^2 v'}{\partial z^2} + M^2 \frac{\partial^2 u'}{\partial x \partial z} - N^2 \frac{\partial^2 u'}{\partial x^2}. \end{aligned} \quad (\text{A.25})$$

This leaves only a v' term left to deal with. Take $\partial^2/\partial z^2$ of (A.14) to get

$$\left(\frac{\partial}{\partial t} - v_h \frac{\partial^2}{\partial x^2} - v_v \frac{\partial^2}{\partial z^2} \right) \frac{\partial^2 v'}{\partial z^2} = -\frac{dV_B}{dx} \frac{\partial^2 u'}{\partial z^2} - f \frac{\partial^2 u'}{\partial z^2} - \frac{dV_G}{dz} \frac{\partial^2 w'}{\partial z^2} \quad (\text{A.26})$$

and substitute the continuity equation (A.16) again to get

$$\left(\frac{\partial}{\partial t} - v_h \frac{\partial^2}{\partial x^2} - v_v \frac{\partial^2}{\partial z^2} \right) \frac{\partial^2 v'}{\partial z^2} = -\frac{dV_B}{dx} \frac{\partial^2 u'}{\partial z^2} - f \frac{\partial^2 u'}{\partial z^2} + \frac{dV_G}{dz} \frac{\partial^2 u'}{\partial x \partial z}. \quad (\text{A.27})$$

Taking $f(\partial/\partial t - \kappa_h \partial^2/\partial x^2 - \kappa_v \partial^2/\partial z^2)$ of (A.27),

$$\begin{aligned} & f \left(\frac{\partial}{\partial t} - v_h \frac{\partial^2}{\partial x^2} - v_v \frac{\partial^2}{\partial z^2} \right) \left(\frac{\partial}{\partial t} - \kappa_h \frac{\partial^2}{\partial x^2} - \kappa_v \frac{\partial^2}{\partial z^2} \right) \frac{\partial^2 v'}{\partial z^2} \\ &= -f \frac{dV_B}{dx} \left(\frac{\partial}{\partial t} - \kappa_h \frac{\partial^2}{\partial x^2} - \kappa_v \frac{\partial^2}{\partial z^2} \right) \frac{\partial^2 u'}{\partial z^2} \\ &- f^2 \left(\frac{\partial}{\partial t} - \kappa_h \frac{\partial^2}{\partial x^2} - \kappa_v \frac{\partial^2}{\partial z^2} \right) \frac{\partial^2 u'}{\partial z^2} \\ &+ \left(\frac{\partial}{\partial t} - \kappa_h \frac{\partial^2}{\partial x^2} - \kappa_v \frac{\partial^2}{\partial z^2} \right) f \frac{dV_G}{dz} \frac{\partial^2 u'}{\partial x \partial z}. \end{aligned} \quad (\text{A.28})$$

Taking the basic state to be in thermal wind balance gives

$$f \frac{dV_G}{dz} = M^2 \quad (\text{A.29})$$

and for brevity one can write $dV_B/dx = \zeta$, where ζ is the vertical component of the relative vorticity of the base flow. These can immediately be substituted into (A.28) to get

$$\begin{aligned} & f \left(\frac{\partial}{\partial t} - v_h \frac{\partial^2}{\partial x^2} - v_v \frac{\partial^2}{\partial z^2} \right) \left(\frac{\partial}{\partial t} - \kappa_h \frac{\partial^2}{\partial x^2} - \kappa_v \frac{\partial^2}{\partial z^2} \right) \frac{\partial^2 v'}{\partial z^2} \\ &= \left(\frac{\partial}{\partial t} - \kappa_h \frac{\partial^2}{\partial x^2} - \kappa_v \frac{\partial^2}{\partial z^2} \right) \left(M^2 \frac{\partial^2 u'}{\partial x \partial z} - (f^2 + f\zeta) \frac{\partial^2 u'}{\partial z^2} \right). \end{aligned} \quad (\text{A.30})$$

One last operation is necessary: taking $(\partial/\partial t - v_h \partial^2/\partial x^2 - v_v \partial^2/\partial z^2)$ of (A.25),

$$\begin{aligned} & \left(\frac{\partial}{\partial t} - v_h \frac{\partial^2}{\partial x^2} - v_v \frac{\partial^2}{\partial z^2} \right)^2 \left(\frac{\partial}{\partial t} - \kappa_h \frac{\partial^2}{\partial x^2} - \kappa_v \frac{\partial^2}{\partial z^2} \right) \frac{\partial^2 u'}{\partial z^2} \\ &= -\beta \left(\frac{\partial}{\partial t} - v_h \frac{\partial^2}{\partial x^2} - v_v \frac{\partial^2}{\partial z^2} \right)^2 \left(\frac{\partial}{\partial t} - \kappa_h \frac{\partial^2}{\partial x^2} - \kappa_v \frac{\partial^2}{\partial z^2} \right) \frac{\partial^2 u'}{\partial x^2} \\ &+ f \left(\frac{\partial}{\partial t} - v_h \frac{\partial^2}{\partial x^2} - v_v \frac{\partial^2}{\partial z^2} \right) \left(\frac{\partial}{\partial t} - \kappa_h \frac{\partial^2}{\partial x^2} - \kappa_v \frac{\partial^2}{\partial z^2} \right) \frac{\partial^2 v'}{\partial z^2} \\ &+ M^2 \left(\frac{\partial}{\partial t} - v_h \frac{\partial^2}{\partial x^2} - v_v \frac{\partial^2}{\partial z^2} \right) \frac{\partial^2 u'}{\partial x \partial z} \\ &- N^2 \left(\frac{\partial}{\partial t} - v_h \frac{\partial^2}{\partial x^2} - v_v \frac{\partial^2}{\partial z^2} \right) \frac{\partial^2 u'}{\partial x^2} \end{aligned} \quad (\text{A.31})$$

and one may now substitute in for the v' term here using (A.30):

$$\begin{aligned} & \left(\frac{\partial}{\partial t} - v_h \frac{\partial^2}{\partial x^2} - v_v \frac{\partial^2}{\partial z^2} \right)^2 \left(\frac{\partial}{\partial t} - \kappa_h \frac{\partial^2}{\partial x^2} - \kappa_v \frac{\partial^2}{\partial z^2} \right) \frac{\partial^2 u'}{\partial z^2} \\ &= -\beta \left(\frac{\partial}{\partial t} - v_h \frac{\partial^2}{\partial x^2} - v_v \frac{\partial^2}{\partial z^2} \right)^2 \left(\frac{\partial}{\partial t} - \kappa_h \frac{\partial^2}{\partial x^2} - \kappa_v \frac{\partial^2}{\partial z^2} \right) \frac{\partial^2 u'}{\partial x^2} \\ &+ \left(\frac{\partial}{\partial t} - \kappa_h \frac{\partial^2}{\partial x^2} - \kappa_v \frac{\partial^2}{\partial z^2} \right) \left(M^2 \frac{\partial^2 u'}{\partial x \partial z} - (f^2 + f\zeta) \frac{\partial^2 u'}{\partial z^2} \right) \\ &+ M^2 \left(\frac{\partial}{\partial t} - v_h \frac{\partial^2}{\partial x^2} - v_v \frac{\partial^2}{\partial z^2} \right) \frac{\partial^2 u'}{\partial x \partial z} \\ &- N^2 \left(\frac{\partial}{\partial t} - v_h \frac{\partial^2}{\partial x^2} - v_v \frac{\partial^2}{\partial z^2} \right) \frac{\partial^2 u'}{\partial x^2}. \end{aligned} \quad (\text{A.32})$$

Now everything is in terms of u' , so consider normal modes (a wave solution) of the form

$$u' = \hat{u} e^{ikx + imz + \sigma t}. \quad (\text{A.33})$$

Substituting (A.33) into (A.32) and eliminating like terms,

$$\begin{aligned} & (\sigma + v_h k^2 + v_v m^2)^2 (\sigma + \kappa_h k^2 + \kappa_v m^2) (-m^2) \\ &= -\beta (\sigma + v_h k^2 + v_v m^2)^2 (\sigma + \kappa_h k^2 + \kappa_v m^2) (-k^2) \\ &+ (\sigma + \kappa_h k^2 + \kappa_v m^2) (M^2 (-km) - (f^2 + f\zeta) (-m^2)) \\ &+ M^2 (\sigma + v_h k^2 + v_v m^2) (-km) \\ &- N^2 (\sigma + v_h k^2 + v_v m^2) (-k^2). \end{aligned} \quad (\text{A.34})$$

Letting the Prandtl number be 1 (i.e. $\kappa_h = v_h$ and $\kappa_v = v_v$), (A.34) simplifies to

$$\begin{aligned} & -(\sigma + v_h k^2 + v_v m^2)^2 m^2 = \beta (\sigma + v_h k^2 + v_v m^2)^2 k^2 \\ & - M^2 km + (f^2 + f\zeta) m^2 \\ & - M^2 km + N^2 k^2. \end{aligned} \quad (\text{A.35})$$

Rearranging, this gives

$$\begin{aligned} & (\sigma + v_h k^2 + v_v m^2)^2 (\beta k^2 + m^2) \\ &= 2M^2 km - (f^2 + f\zeta) m^2 - N^2 k^2 \end{aligned} \quad (\text{A.36})$$

and the growth rate σ is

$$\sigma = \left[\frac{2M^2 km - (f^2 + f\zeta) m^2 - N^2 k^2}{\beta k^2 + m^2} \right]^{1/2} - (v_h k^2 + v_v m^2). \quad (\text{A.37})$$

A.1. Cases

A.1.1. Case 1: inviscid, hydrostatic

Setting $\beta = 0$, $v_h = 0$, and $v_v = 0$, (A.37) becomes

$$\sigma = \left[\frac{2M^2 km - (f^2 + f\zeta) m^2 - N^2 k^2}{m^2} \right]^{1/2}, \quad (\text{A.38})$$

which simplifies to

$$\sigma = \left[\frac{M^4}{N^2} - (f^2 + f\zeta) - N^2 \left(\frac{k}{m} - \frac{M^2}{N^2} \right)^2 \right]^{1/2}. \quad (\text{A.39})$$

A.1.2. Case 2: viscous, hydrostatic

Setting $\beta = 0$ but keeping the viscous terms, (A.37) becomes

$$\sigma = \left[\frac{2M^2 km - (f^2 + f_\zeta)m^2 - N^2 k^2}{m^2} \right]^{1/2} - (v_h k^2 + v_v m^2), \quad (\text{A.40})$$

which simplifies to

$$\sigma = \left[\frac{M^4}{N^2} - (f^2 + f_\zeta) - N^2 \left(\frac{k}{m} - \frac{M^2}{N^2} \right)^2 \right]^{1/2} - (v_h k^2 + v_v m^2). \quad (\text{A.41})$$

If the viscosity is isotropic ($v_h = v_v$), the solution is the same as in Taylor and Ferrari (2009).

A.1.3. Case 3: inviscid, nonhydrostatic

Setting $\beta = 1$ gives us the nonhydrostatic solution, and here we set $v_h = v_v = 0$:

$$\sigma = \left[\frac{2M^2 km - (f^2 + f_\zeta)m^2 - N^2 k^2}{k^2 + m^2} \right]^{1/2}. \quad (\text{A.42})$$

Dividing the numerator and denominator by m^2 gives the alternative form

$$\sigma = \left[\frac{M^4}{N^2} - (f^2 + f_\zeta) - N^2 \left(\frac{k}{m} - \frac{M^2}{N^2} \right)^2 \right]^{1/2} \left(1 + \frac{k^2}{m^2} \right)^{-1/2}, \quad (\text{A.43})$$

which reduces to the inviscid, hydrostatic growth rate in the limit where $k^2/m^2 \ll 1$.

A.1.4. Case 4: viscous, nonhydrostatic

Setting $\beta = 1$ and retaining the viscous terms, we have

$$\sigma = \left[\frac{2M^2 km - (f^2 + f_\zeta)m^2 - N^2 k^2}{k^2 + m^2} \right]^{1/2} - (v_h k^2 + v_v m^2). \quad (\text{A.44})$$

Performing the same simplification as in (A.43), this can be rewritten

$$\sigma = \left[\frac{M^4}{N^2} - (f^2 + f_\zeta) - N^2 \left(\frac{k}{m} - \frac{M^2}{N^2} \right)^2 \right]^{1/2} \left(1 + \frac{k^2}{m^2} \right)^{-1/2} - (v_h k^2 + v_v m^2). \quad (\text{A.45})$$

References

- Allen, J.S., Newberger, P.A., 1998. On symmetric instabilities in oceanic bottom boundary layers. *J. Phys. Oceanogr.* 28 (6), 1131–1151.
- Bewley, T., 2010. Numerical Renaissance: Simulation, Optimization, and Control. Renaissance, San Diego, CA <<http://numerical-renaissance.com>>.
- Boccaletti, G., Ferrari, R., Fox-Kemper, B., 2007. Mixed layer instabilities and restratification. *J. Phys. Oceanogr.* 37 (9), 2228–2250.
- Capet, X., McWilliams, J.C., Molemaker, M.J., Shchepetkin, A.F., 2008a. Mesoscale to submesoscale transition in the California current system. Part I: Flow structure, eddy flux, and observational tests. *J. Phys. Oceanogr.* 38 (1), 29–43.
- Capet, X., McWilliams, J.C., Molemaker, M.J., Shchepetkin, A.F., 2008b. Mesoscale to submesoscale transition in the California current system. Part II: Frontal processes. *J. Phys. Oceanogr.* 38 (1), 44–64.
- Capet, X., McWilliams, J.C., Molemaker, M.J., Shchepetkin, A.F., 2008c. Mesoscale to submesoscale transition in the California current system. Part III: Energy balance and flux. *J. Phys. Oceanogr.* 38 (10), 2256–2269.
- Delworth, T., Rosati, A., Anderson, W., Adcroft, A., Balaji, V., Benson, R., Dixon, K., Griffies, S., Lee, H., Pacanowski, R., Vecchi, G.A., Wittenberg, A.T., Zeng, F., Zhang, R., 2012. Simulated climate and climate change in the GFDL CM2.5 high-resolution coupled climate model. *J. Climate* 25, 2755–2781.
- Emanuel, K.A., 1994. Atmospheric Convection. Oxford University Press.
- Fox-Kemper, B., Ferrari, R., Hallberg, R., 2008. Parameterization of mixed layer eddies. Part I: Theory and diagnosis. *J. Phys. Oceanogr.* 38 (6), 1145–1165.
- Griffiths, S.D., 2003. Nonlinear vertical scale selection in equatorial inertial instability. *J. Atmos. Sci.* 60 (7).
- Haine, T.W.N., Marshall, J.C., 1998. Gravitational, symmetric and baroclinic instability of the ocean mixed layer. *J. Phys. Oceanogr.* 28, 634–658.
- Henning, C.C., Vallis, G.K., 2004. The effects of mesoscale eddies on the main subtropical thermocline. *J. Phys. Oceanogr.* 34 (11), 2428–2443.
- Holton, J.R., Hakim, G.J., 2012. An Introduction to Dynamic Meteorology. Academic Press.
- Hoskins, B.J., 1974. The role of potential vorticity in symmetric stability and instability. *Quart. J. R. Meteorol. Soc.* 100 (425), 480–482.
- Joyce, T.M., Toole, J.M., Klein, P., Thomas, L.N., 2013. A near-inertial mode observed within a Gulf Stream warm-core ring. *J. Geophys. Res.* 118, 1797–1806.
- Klein, P., Hua, B.L., Lapeyre, G., Capet, X., Le Gentil, S., Sasaki, H., 2008. Upper ocean turbulence from high-resolution 3D simulations. *J. Phys. Oceanogr.* 38 (8), 1748–1763.
- Large, W.G., McWilliams, J.C., Doney, S.C., 1994. Oceanic vertical mixing: a review and a model with a nonlocal boundary layer parameterization. *Rev. Geophys.* 32 (4), 363–403.
- Li, K., Zhang, Z., Chini, G., Flierl, G., 2012. Langmuir circulation: an agent for vertical restratification? *J. Phys. Oceanogr.* 42 (11), 1945–1958.
- Mahadevan, A., 2006. Modeling vertical motion at ocean fronts: are nonhydrostatic effects relevant at submesoscales? *Ocean Modell.* 14 (3), 222–240.
- Mahadevan, A., Tandon, A., 2006. An analysis of mechanisms for submesoscale vertical motion at ocean fronts. *Ocean Modell.* 14 (3), 241–256.
- Marshall, J., Adcroft, A., Hill, C., Perelman, L., Heisey, C., 1997. A finite-volume, incompressible Navier–Stokes model for studies of the ocean on parallel computers. *J. Geophys. Res.* 102 (C3), 5753–5766.
- Marshall, J., Hill, C., Perelman, L., Adcroft, A., 1997. Hydrostatic, quasi-hydrostatic, and nonhydrostatic ocean modeling. *J. Geophys. Res.: Oceans* (1978–2012) 102 (C3), 5733–5752.
- Molemaker, M.J., McWilliams, J.C., Yavneh, I., 2005. Baroclinic instability and loss of balance. *J. Phys. Oceanogr.* 35 (9), 1505–1517.
- Orszag, S.A., 1971. On the elimination of aliasing in finite-difference schemes by filtering high-wavenumber components. *J. Atmos. Sci.* 28 (6), 1074, 1074.
- Smagorinsky, J., 1963. General circulation experiments with the primitive equations: I. The basic experiment. *Mon. Weather Rev.* 91 (3), 99–164.
- Smagorinsky, J., 1993. Some historical remarks on the use of nonlinear viscosities. *Large Eddy Simul. Complex Eng. Geophys. Flows* 1, 69–106.
- Spall, M.A., 1995. Frontogenesis, subduction, and cross-front exchange at upper ocean fronts. *J. Geophys. Res.: Oceans* (1978–2012) 100 (C2), 2543–2557.
- Stone, P.H., 1966. On non-geostrophic baroclinic stability. *J. Atmos. Sci.* 23 (4), 390–400.
- Stone, P.H., 1970. On non-geostrophic baroclinic stability: Part II. *J. Atmos. Sci.* 27 (5), 721–726.
- Taylor, J.R., 2008. Numerical Simulations of the Stratified Oceanic Bottom Boundary Layer (Ph.D. thesis). University of California, San Diego, 212 p.
- Taylor, J.R., Ferrari, R., 2009. On the equilibration of a symmetrically unstable front via a secondary shear instability. *J. Fluid Mech.* 622 (1), 103–113.
- Taylor, J.R., Ferrari, R., 2010. Buoyancy and wind-driven convection at mixed layer density fronts. *J. Phys. Oceanogr.* 40 (6), 1222–1242.
- Thomas, L.N., 2005. Destruction of potential vorticity by winds. *J. Phys. Oceanogr.* 35, 2457–2466.
- Thomas, L.N., Ferrari, R., 2008. Friction, frontogenesis, and the stratification of the surface mixed layer. *J. Phys. Oceanogr.* 38 (11), 2501–2518.
- Thomas, L.N., Lee, C.M., 2005. Intensification of ocean fronts by down-front winds. *J. Phys. Oceanogr.* 35, 1086–1102.
- Thomas, L.N., Taylor, J.R., 2010. Reduction of the usable wind-work on the general circulation by forced symmetric instability. *Geophys. Res. Lett.* 37 (18), L18606.
- Thomas, L.N., Tandon, A., Mahadevan, A., 2008. Submesoscale processes and dynamics. *Ocean Modeling in an Eddying Regime*, pp. 17–38.
- Thomas, L.N., Taylor, J.R., Ferrari, R., Joyce, T.M., 2013. Symmetric instability in the Gulf Stream. *Deep Sea Research Part II: Topical Studies in Oceanography*.
- Thorpe, A.S., Rotunno, R., 1989. Nonlinear aspects of symmetric instability. *J. Atmos. Sci.* 46 (9), 1285–1299.
- Van Roekel, L.P., Hamlington, P.E., Fox-Kemper, B., 2012. Multiscale simulations of Langmuir cells and submesoscale eddies using XSEDE resources. In: *Proceedings of the 1st Conference of the Extreme Science and Engineering Discovery Environment: Bridging from the eXtreme to the Campus and Beyond*. ACM, p. 20.
- Whitt, D.B., Thomas, L.N., 2013. Near-inertial waves in strongly baroclinic currents. *J. Phys. Oceanogr.* 43 (4), 706–725.